Nanoscale Imaging of Photocurrent and Efficiency in CdTe Solar Cells

Marina S. Leite,[*,†,‡,§] Maxim Abashin,[‡,§] Henri J. Lezec,[‡] Anthony Gianfrancesco,[‡] A. Alec Talin,[‡,∥] and Nikolai B. Zhitenev[‡]

[†]Department of Materials Science and Engineering, Institute for Research in Electronics and Applied Physics, University of Maryland, College Park, Maryland 20742 United States, [‡]Center for Nanoscale Science and Technology, NIST, Gaithersburg, Maryland 20899 United States, [§]Maryland Nanocenter at the University of Maryland, College Park, Maryland 20742 United States, and [∥]Sandia National Laboratories, Livermore, California 94550 United States

ABSTRACT The local collection characteristics of grain interiors and grain boundaries in thin-film CdTe polycrystalline solar cells are investigated using scanning photocurrent microscopy. The carriers are locally generated by light injected through a small aperture (50−300 nm) of a near-field scanning optical microscope in an illumination mode. Possible influence of rough surface topography on light coupling is examined and eliminated by sculpting smooth wedges on the granular CdTe surface. By varying the wavelength of light, nanoscale spatial variations in external quantum efficiency are mapped. We find that the grain boundaries (GBs) are better current collectors than the grain interiors (GIs). The increased collection efficiency is caused by two distinct effects associated with the material composition of GBs. First, GBs are charged, and the corresponding built-in field facilitates the separation and the extraction of the photogenerated carriers. Second, the GB regions generate more photocurrent at long wavelength corresponding to the band edge, which can be caused by a smaller local band gap. Resolving carrier collection with nanoscale resolution in solar cell materials is crucial for optimizing the polycrystalline device performance through appropriate thermal processing and passivation of defects and surfaces.

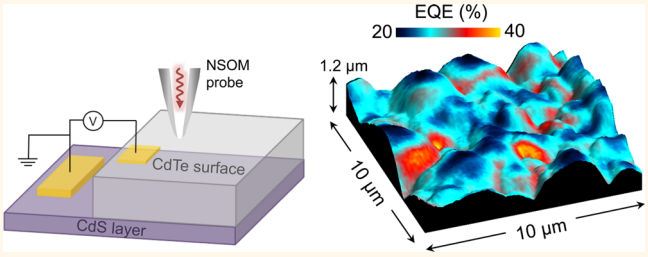

KEYWORDS: photovoltaics · CdTe · scanning photocurrent microscopy · solar cells · NSOM

Effective, high-efficiency, *and* low-cost photovoltaics represent the "holy grail" technology to successfully eliminate our dependence on fossil fuels. Thin-film polycrystalline materials are attractive for manufacturing low-cost PV modules, but improvements in efficiency are still required to ensure cost competitiveness. In particular, CdTe/CdS heterojunction solar cells are the leading technology in the thin-film PV market today. This success is primarily based on the inherently simple and low-cost deposition method used to produce these modules with manufacturing cost as low as $0.6/W.[1,2]

Despite having similar optical properties, polycrystalline thin-film CdTe devices consistently show lower V_{oc} when compared, for example, to GaAs single-crystal solar cells, which hold a record $V_{oc} = 1.122$ V[2] (for both direct band gap materials $E_g = 1.4$ eV and absorption coefficient $\alpha \approx 3.0 \times 10^4$ cm^{-1} to 9.0×10^4 cm^{-1} at 650 nm). This lower performance is primarily caused by the high density of nonradiative recombination centers within polycrystalline CdTe. The V_{oc} of the best CdTe solar cells is currently limited at 0.86 V, which is considerably below the theoretical predictions,[3,4] leading to an efficiency of 18.7%.[2,4] For large-area modules, the current V_{oc} record is 0.90 V, with an efficiency record of 16.1% under global AM1.5 illumination.[5]

The polycrystalline CdTe absorber layer in a PV device is composed of grains ≈1 μm in diameter, as shown by the scanning electron microscopy (SEM) image for a p-type CdTe layer in Figure 1a and Figure SOM-1 in Supporting Information. It is not surprising that the properties of the grain interiors (GIs) can be quite different from those of the grain boundaries (GBs). The GBs accumulate microscopic defects, such as dislocations, vacancies, and distorted bonds, which can strongly affect the transport properties of both majority and minority carriers. Figure 1b shows an atomic resolution transmission electron microscopy (TEM) image of a sharp interface between two CdTe grains,

* Address correspondence to mleite@umd.edu.

Received for review September 17, 2014 and accepted October 15, 2014.

Published online October 15, 2014
10.1021/nn5052585

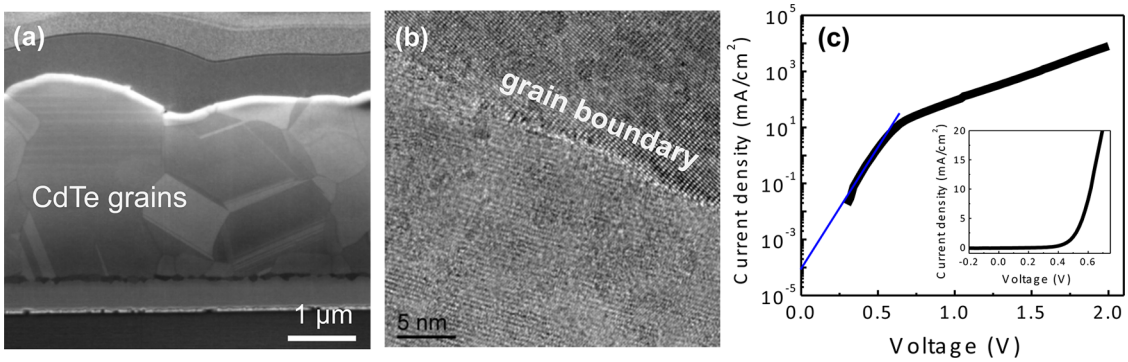

Figure 1. CdTe polycrystalline solar cells. (a) Cross-section SEM image of a thin-film CdTe solar cell showing micron-scale grains and interfaces with structural defects. (b) Atomic resolution TEM image showing a grain boundary (interface between two grains). (c) Semilog dark *I*−*V* curve. The blue line corresponds to the fit used to infer the shunt current. Inset: linear dark *I*−*V* showing diode behavior of CdTe/CdS solar cell device.

which have been shown to introduce electronic states within the band gap and, consequently, significant trap-assisted recombination and/or band bending.[6] Recently, it has been shown that during the conventional $CdCl_2$ chemical treatment used to improve the devices[7,8] Cl atoms replace Te which also leads to local band bending.[6] For a p-type material, these gap states (or "trap states") are spatially localized and trap holes, resulting in an accumulation of positive charges at the boundaries (as represented in Supporting Information Figure SOM-2).

The highest V_{oc} reported for CdTe solar cells, 0.86 to 0.91 V,[9] was achieved by using single-crystalline p-CdTe, instead of a polycrystalline layer. The significant lowering of [qV_{oc}] in polycrystalline CdTe is caused by a leakage (or shunt) current when a PV diode is forward biased (*e.g.*, Figure 1c), which can be partially associated with the device micro/nanostructure and the presence of the GBs. Therefore, measuring the electrical properties of the GBs and the GIs exposed to different chemical treatments that passivate the CdTe layer has been the emphasis of multiple studies aiming to increase V_{oc} (>1.0 V) and improve device performance.[8,10−16] Here, we focus on mapping the local electrical characteristics of the GIs and GBs by spatially and spectrally resolving the generated photocurrent and the external quantum efficiency (EQE) in the semiconductor material with nanoscale resolution. For that, we use near-field scanning optical microscopy (NSOM) probes as a local source of illumination/excitation.

To date, scanning probe microscopy techniques have been extensively used to map structural and electrical properties of polycrystalline solar cells.[12,13,17−22] In particular, atomic force microscopy and scanning tunneling microscopy have been used to explain the beneficial role of the GBs in CdTe solar cells for photocurrent collection, which is attributed to both the built-in electric fields[17,23−25] and composition variations within the polycrystalline grains.[26−29] Further, NSOM fiber-based apertured probes have allowed the identification of relative changes in local photoresponse of solar cells by means of scanning photocurrent microscopy,[30−33] which is particularly useful for characterizing inhomogeneous materials, such as organic and thin-film polycrystalline solar cells.

Here, we use scanning photocurrent microscopy (SPCM) to image the local electronic properties of CdTe solar cells. We spatially and spectrally resolve the photocurrent distribution and the EQE within the CdTe polycrystalline layer of the solar cell while mimicking the power density operation conditions of real devices. Possible topography effects are addressed by sculpting shallow-angle wedges on the originally rough CdTe grains. The use of the wedge geometry also offers a pathway for spectroscopic photocurrent tomography of the device through assembling and quantifying photocurrent maps at different wavelengths and absorber thickness. We find that the GBs are consistently better current collectors compared to GIs. At short wavelengths (<600 nm), when light is absorbed near the exposed surface, the EQE is relatively small because of surface recombination. However, we find that the GBs significantly outperform the GIs due to built-in field facilitating the separation and extraction of electrons and holes. This result also suggests that nonradiative recombination at well-passivated GBs is relatively small. Close to the material band gap (860 nm), the EQE enhancement at the GBs is found to be $\times$1.5. The latter effect can be attributed to the higher absorption at the GBs due to smaller band gap caused by compositional variations.

RESULTS AND DISCUSSION

Figure 2 shows (a) topography and (b) photocurrent maps of a representative region of the CdTe solar cell. The experimental setup used for the nanoscale SPCM measurements is described in detail in the Methods section and Supporting Information Figure SOM-3. During the scan, the light source (532 nm) was successively turned "on" and "off" to confirm that the photocurrent signal was being exclusively generated by the

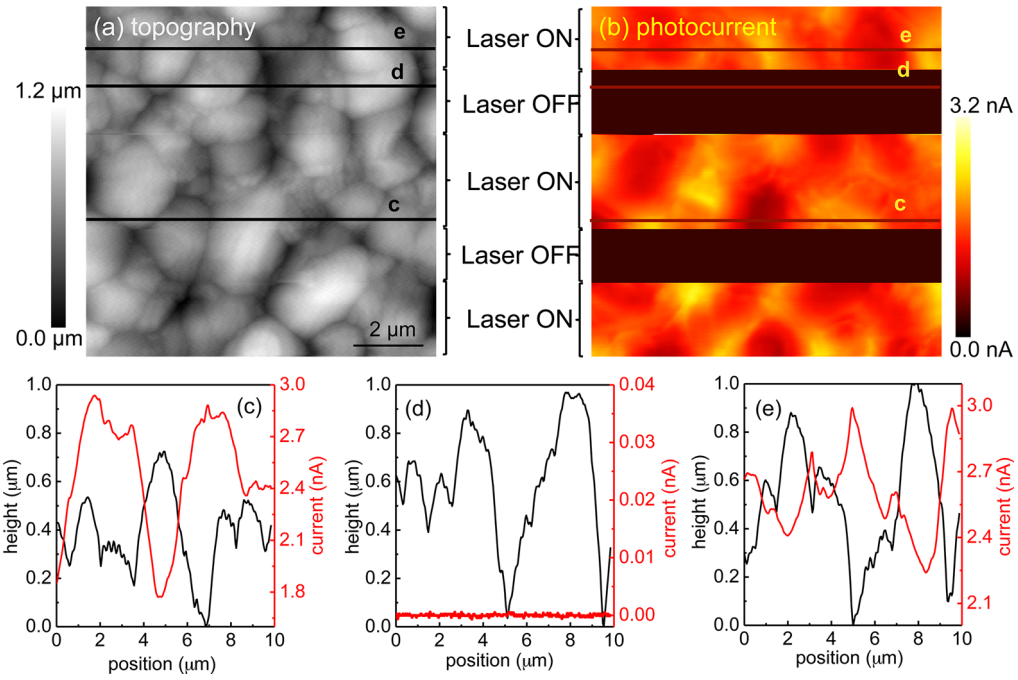

Figure 2. Nanoscale scanning photocurrent microscopy. (a) Topography and (b) photocurrent maps of a representative region of the CdTe solar cell. Line profiles of topography (black) and photocurrent (red), as indicated in (a,b), for light source (c) on, (d) off, and (e) on again. During scan: set point = 0.8−1.1 V; illumination source = 532 nm laser; incident laser power = 3.5 nW; NSOM probe = 200 nm.

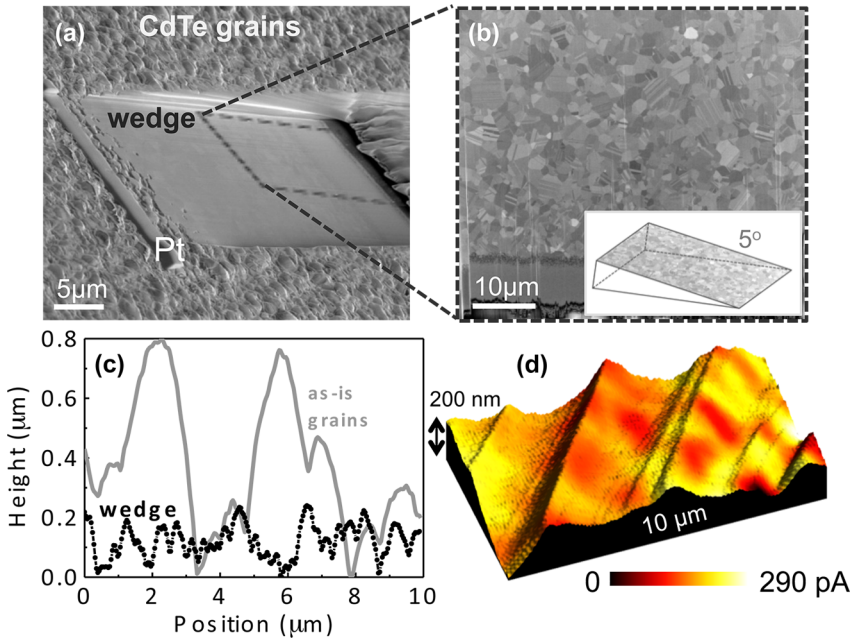

Figure 3. Analysis of topographic effects in nanoscale photocurrent scanning microscopy. (a,b) SEM images of wedge sculpted by Ga focused ion beam. Inset shows a schematic of the wedge shape. (c) Surface topography of CdTe grains before (as-is grains) and after (wedge) the milling process. (d) Three-dimensional topography overlaid with photocurrent measurement. Illumination source = 532 nm laser; incident power = 0.5 nW; NSOM probe = 200 nm. For the topography scan, set point = 0.95 V.

local excitation source (NSOM probe), as indicated by the line scan profiles of Figure 2c−e. The line profiles of topography and photocurrent displayed in Figure 2e are anticorrelated. Since GBs appear as topographical depressions in line scans, the result in Figure 2e illustrates that the GBs are better photocurrent collectors than the GIs. The noise level of the current signal in the dark (Figure 2d) was used to infer the uncertainty of the photocurrent measurements, which is ≈1.3 pA. The listed light power is the power emitted by the NSOM probe, and in all cases, it corresponds to a low injection level, mimicking realistic conditions of solar cells'

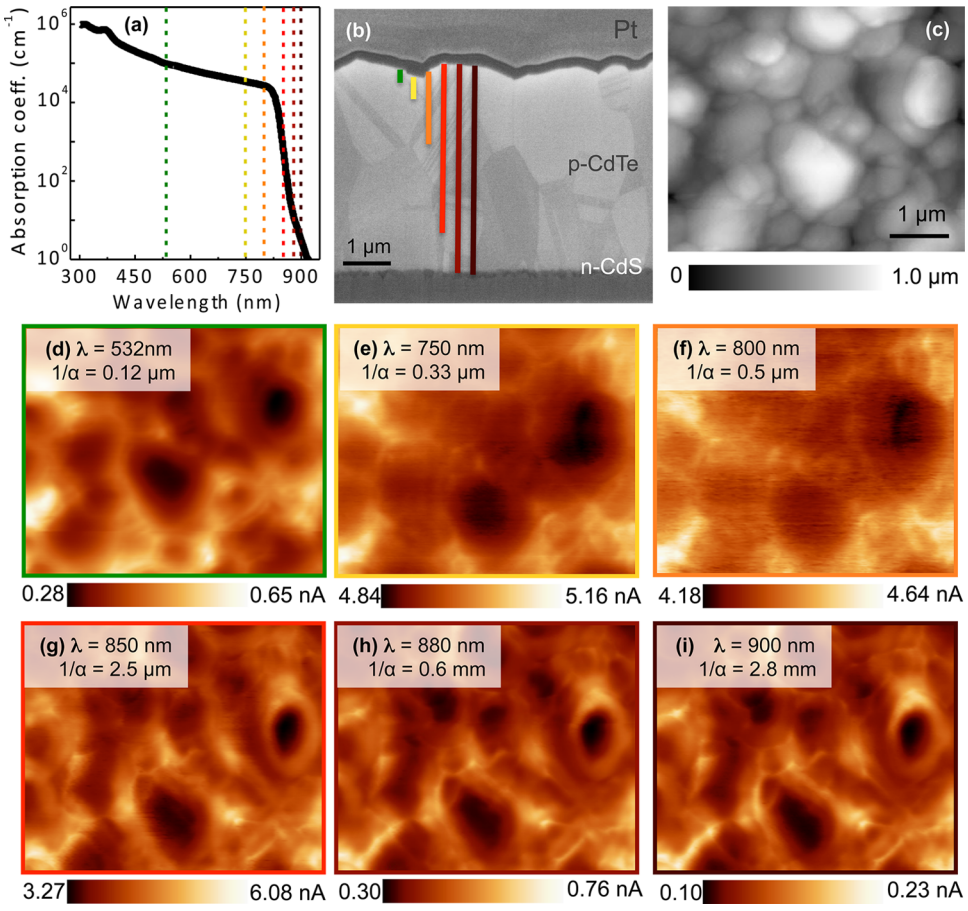

Figure 4. Photocurrent tomography of CdTe solar cell. (a) Absorption coefficient α as a function of wavelength for CdTe. (b) Cross-section SEM image showing light absorption as a function of the distance to the p−n junction. Pt layer is used to protect the surface of CdTe during the milling process. The lines schematically illustrate the penetration depths (1/α) for the corresponding wavelengths. (c) Topography scan using set point = 0.75 to 0.85 V. (d−i) Photocurrent microscopy measurements of the p-CdTe layer under different illumination wavelengths (λ). The current scale was adjusted to clearly show the contrast between GIs and GBs in all images. Incident laser power = 1.0 nW; NSOM probe = 300 nm.

operation. Because the CdTe layer does not contain an antireflection coating, we expect at least 30% of the light to be reflected and not absorbed.

We note that the as-prepared CdTe surface is topographically rough, which can complicate interpretation of SPCM measurements. To examine the possible influence of topography on the photogenerated current signal, a wedge with ≈5° angle was sculpted by focused ion beam on the surface of the CdTe grains, as shown in Figure 3a. Low beam current (1.0 nA) was used to minimize the surface damage and to preserve the crystalline property of the material, as seen in Figure 3b. Electron backscattering diffraction measurements of the wedge and of the as-grown adjacent regions presented similar distributions of the grain orientations, confirming that the wedge did not modify the polycrystalline nature of the sample, as desired (see Figure SOM-4). The wedge line profile has a residual roughness associated with the "curtain effect" produced by the ion beam of ≈0.2 μm, in contrast with the original grain roughness of (≈1.0 μm) uncorrelated with the local grain structure, as displayed in Figure 3c. Despite the modified topography of the grains, the photocurrent of the device showed a nonuniform current distribution (Figure 3d), in accordance with the measurements performed on the unmodified grains. These measurements further confirm that the photocurrent is not strongly affected by the topography and that the GBs are indeed more efficient current collectors compared to the GIs.

The spectrally resolved SPCM measurements on the same region of the specimen allow us to probe different volumes of the device, in accordance with the absorption coefficient α of CdTe (Figure 4a), and to create a tomographic map of the photocurrent. Figure 4b illustrates the sampled volume of the CdTe device at different excitation wavelengths. The nanoscale spatially resolved photocurrent maps were acquired by controlling the power and the wavelength of the incoming light through the NSOM probe. For that, a supercontinuum laser source and appropriate filters were used, as explained in detail in the Methods section. For all nanoscale SPCM measurements, the topography signal was simultaneously acquired

(Figure 4c). At short wavelengths (λ = 532 nm, Figure 4d), most of the light is absorbed within the first 100 nm of the exposed material. The overall spatial contrast is similar to that presented in Figure 2, with the GBs showing higher collection efficiency. The photocurrent is generated far from the p−n junction and is likely limited by the surface recombination processes and by the recombination within the CdTe layer. For longer wavelengths (Figure 4e,f, λ = 600−800 nm), the volume closer to the p−n junction is excited and the overall photocurrent is increased. However, the signal is averaged over a larger excitation volume, and the contrast between the GBs and the GIs is diminished.

Unexpectedly, at excitation wavelengths close to the band gap energy of CdTe (E_g = 1.44 eV, λ = 860 nm), the contrast between the GBs and the GIs increases again even though the excitation volume grows larger. At this wavelength, $\alpha = 1.3\ cm^{-1}$ for CdTe. At energies below the band gap (Figure 4h,i), the absorption quickly vanishes (Figure 4a), resulting in a significant reduction of the generated photocurrent. The contrast between GBs and GIs, however, remains strong. This sharp contrast may be caused by stoichiometry variations at the GBs, resulting in smaller band gap and, therefore, in higher absorption; however, the accurate and unambiguous determination of the chemical composition of the GBs requires the use of high-resolution destructive techniques, such as atom probe tomography.[34]

One of the primary figures of merit of a PV device is the EQE, defined as the number of charge carriers produced by the solar cell per photons incident on the device. Macroscale measurements of EQE are valuable to diagnose how effectively the device is converting sunlight into electricity along the spectrum. Nevertheless, for inhomogeneous materials such as CdTe, the contribution of GBs and GIs to the EQE can strongly depend on variations in composition and on the transport properties found within the different grains and interfaces. Here, we use the nanoscale SPCM measurements to spatially resolve the EQE of the CdTe GBs and GIs, which is defined according to the following equation:

$$\mathrm{EQE} = \left(\frac{hc}{q}\right)\frac{1}{\lambda}\left(\frac{I}{P}\right) \qquad (1)$$

where h is Planck's constant, c is the speed of light in vacuum, q is the electronic charge, λ is the excitation wavelength, I is the generated photocurrent, and P is the incident power or photon flux. The generated current I and the incident power P are determined directly from the photocurrent measurements and power source calibration, respectively.

In order to characterize the collection characteristics of the CdTe layer, we spatially and spectrally map the EQE of the GBs, GIs, and the grain sides (GSs) over a broad region of the spectrum, as shown in Figures 5 and SOM-5. The GSs have a topography distinct from GIs caused by the remarkable height variation of the

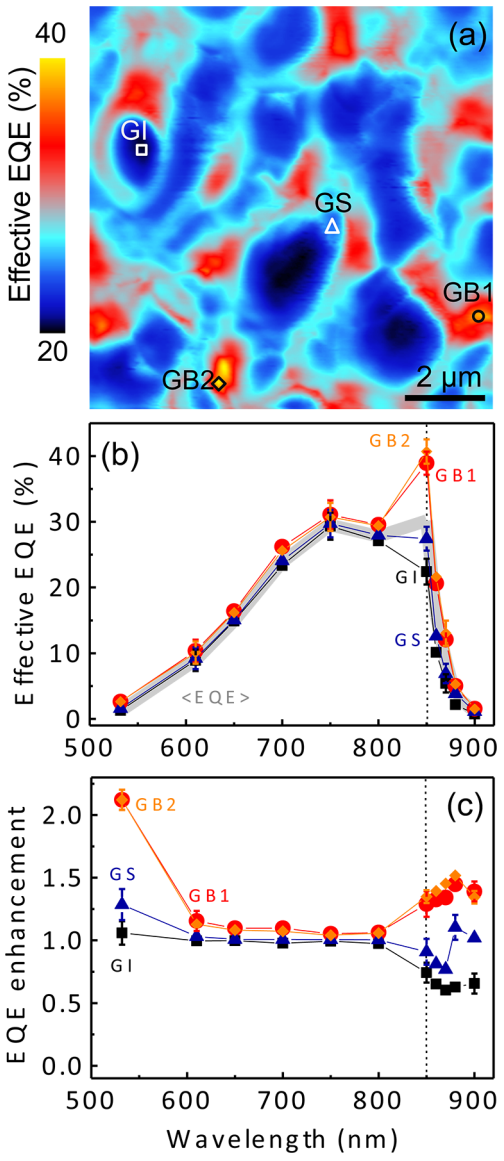

Figure 5. Mapping local variations in EQE with nanoscale resolution. (a) Effective EQE map for CdTe solar cell acquired using 850 nm wavelength as a local excitation source. (b) Effective EQE as a function of wavelength for selected regions of the CdTe layer. (c) EQE enhancement for the same region. GI, grain interior (black); GS, grain side (blue); GB, grain boundary (red, orange). The dashed line corresponds to the CdTe band gap. The error bars correspond to the standard deviation of three measurements, taken at each wavelength.

CdTe grains. The EQE map for λ = 850 nm displayed in Figure 5a shows significant spatial variations. The average EQE (Figure 5b, gray solid line) was determined by integrating over the scanned area of 10 × 10 μm^2. At short wavelengths (≈500 nm), the GBs demonstrate nearly 2-fold enhancement in collection efficiency when compared to the average EQE for the scanned area. The average EQE is limited by surface and bulk recombination as light is absorbed far from the p−n junction of the device. For 600 to 750 nm, the EQE steadily increases, reaching ≈30% with no significant difference between

the GBs, the GSs, and the GIs. The contrast between the GIs, as well as GSs, and GBs emerges again near 800 nm and remains nearly unchanged even as the EQE rapidly diminishes at the band edge.

In general, there are two main contributing processes that must be taken into account in analyzing the SPCM measurements. The first process is the light absorption and carrier generation, which varies as a function of the wavelength of the incident light. The absorption volume increases at longer wavelengths with a sharp increase at the wavelength corresponding to the band edge. The second process is related to carrier recombination. Recombination losses can be very different near the exposed surface (surface recombination), neutral region of the CdTe absorber, depletion region, and near the metallurgical p−n junction. The photocurrent contrast between GSs and GIs at different wavelengths can originate from different contributions. The GS and GI most likely share similar chemical composition but different topography. The contrast in the current signal behaves like the GIs; no significant difference was found between these two situations. The relative EQE enhancement (defined here as the enhancement over the spatial average) at the GBs for short wavelengths ($\lambda < 600$ nm, Figure 5c) is likely a direct consequence of the local built-in electric field facilitating the carrier separation and, therefore, competing with the recombination (both recombination in the "neutral" region of CdTe and surface recombination). This mechanism of the enhancement of photocurrent at the GBs has been reported and discussed in electron-beam-induced current experiments[35,6] and in previous NSOM experiments.[29,36] For 600 nm $< \lambda <$ 800 nm, the difference between light injection to the GBs and GIs and GSs is insignificant. There, the excitation volume is larger and the contrast averages out. Close to the CdTe band gap, despite an even larger excitation volume, light injection at the GBs results in a larger photocurrent, and the EQE is enhanced at the boundaries by ≈50%. The contrast enhancement is clearly associated with proximity of the excitation energy to the band gap: the onset of the contrast enhancement as a function of the wavelength is rather sharp, and the contrast remains strong even as the overall photocurrent decreases significantly at longer wavelengths. We suggest that the measured photocurrent enhancement at GBs in this wavelength range is caused by an increase in absorption relative to the GIs. This means that the band gap at GBs is effectively smaller due to accumulation of impurities and defects, as previously suggested by Smith *et al.*[37] As expected, beyond the material band gap ($\lambda > 860$ nm), the EQE decays rapidly, and the light-generated photocurrent can be eventually associated with trap states within the CdTe band gap.

The strong contrast of the photocurrent enhancement at the GBs and its peculiar dependence on the excitation wavelength allowed us to identify two distinct mechanisms for the observed enhancement. In general, a meaningful comparison of photocurrent maps measured at different wavelengths is a complicated problem. On one hand, local spectroscopic measurements could be sensitive to the variation of composition and spatial distribution of electronic states such as defects and traps. However, at the same time, the sampled volume is changing in accordance with the absorption coefficient, affecting the averaging and the spatial resolution. Additionally, in a PV device, both the recombination and the collection efficiencies vary strongly with the penetration depth toward the p−n junction. Shaping a thin-film PV device in a wedge structure as described above, by gradually varying the thickness of absorber and the distance between the surface and the p−n junction, can offer more opportunities for a three-dimensional spectroscopic tomography of different volumes and interfaces of PV devices with high spatial resolution. For example, the spatial resolution at $\lambda = 532$ nm is limited by the absorption length at ≈100 nm, and the SPCM measurements of thinner areas of the wedge can enable high-resolution mapping of properties within the depletion region and close to the metallurgical p−n junction (see Figure SOM-6). Such measurements can help identify the recombination and leakage mechanism related to material inhomogeneity that currently limits the V_{oc} in thin-film PV materials. We have observed that, for a short wavelength (*e.g.*, $\lambda = 532$ nm), the spatially averaged EQE increases descending down the wedge. This is expected since the generation volume is approaching the depletion region with higher collection efficiency. Correspondingly, the maximum in EQE shifts to shorter wavelengths (see Figure SOM-6). However, further study is needed to more quantitatively relate the spatial variation of the SPCM signal with specimen thickness and determine effects of the wedge fabrication on surface recombination.

CONCLUSIONS

Summarizing, we mapped and quantified the photocurrent generated by CdTe/CdS solar cells GBs and GIs under different illumination conditions by means of nanoscale-resoled SPCM. CdTe wedges were milled and measured to exclude possible artifacts caused by surface topography on coupling of the near-field localized light source. A photocurrent tomography of the CdTe layer was built by spectrally resolving the light-generated current, which consistently showed that the GBs are more efficient current collectors compared to GIs. The nanoscale resolution maps of the EQE inferred from the photocurrent scans revealed that at short wavelengths ($\lambda < 600$ nm) the GBs outperform the GIs by more than a factor of 2, independent of the grain orientation. Surprisingly, close to the material band gap, the difference in EQE was less than 1.5.

We further demonstrated that SPCM of the sample in wedge geometry can be used to probe the photoelectronic properties of critical device volumes such as the depletion region and p−n junction with high spatial resolution. EQE variation at these interfaces helps identify the mechanisms, which limit thin-film PV device efficiency.

METHODS

Sample Preparation. The commercially available CdTe solar cells used in this study are formed by the following layers (from top to bottom): 4.0 mm of glass substrate, 550 nm of bilayer transparent conductive oxide (TCO), 50 nm of n-type CdS, and 3.5 μm of p-type CdTe (see Supporting Information Figure SOM-1). Holes (p) and electrons (n) are majority and minority carriers, respectively. All samples were submitted to $CdCl_2$ treatment. The grains composing the CdTe layer (3.5 μm thick) are 1−2 μm in size with no preferential crystallographic orientation.[17] The original back contact was manually removed by peeling it off of the CdTe layer. No antireflection coating was added. The 100 nm thick platinum pads were evaporated through stencil masks and used as top contacts.

Electrical Measurements. Dark *I*−*V* curves were obtained by contacting the top and the bottom of the solar cells using tungsten probes in a conventional probe station. A voltage sweep from −0.5 to +2.0 V was applied to the device, using steps of 0.1 V per second.

Photocurrent Imaging. Topography and photocurrent were acquired simultaneously using a *XYZ* piezostage with *Z* feedback control, where the average distance between the sample surface and the probe was ∼10 nm for all measurements. To vary the incident light wavelength, either an optical parametric oscillator laser or a supercontinuum laser with the appropriate combination of band-pass filters (10 nm bandwidth) and neutral density filters was used (see schematic of experimental setup in Supporting Information Figure SOM-3). The subwavelength NSOM probes used in this work were tapered optical fiber probes mounted on a tuning fork with 200−300 nm core aperture within a 20 nm Cr/200 nm Au cladding, force constant ∼ 15 N/m, and resonance frequency ≈ 150 kHz. Nanoscale spatial resolution was achieved by placing the tapered fiber probes close to the surface of the grains, therefore providing a local source of excitation. Because of the superstrate geometry of the devices, light was injected in the exposed p-doped CdTe grains. Because this layer does not have an antireflection coating, we expect at least 30% of the incident light to be reflected. The NSOM tip was positioned off the edge of Pt contact (<10 μm) (see SOM-3). The removal of the original back contact metallization by manually peeling the layer off allowed for the tip placement in a closer proximity to the CdTe surface to improve the spatial resolution. Thus, the resolution was primarily determined by the probe diameter and the materials' absorption coefficient α, as explained in the text. The photocurrent signal was amplified by a low-noise variable gain amplifier operating at 10^7 to 10^9 V/A gain.

The laser power was calibrated after transmission through the NSOM probes at both near- and far-field. The power in the near-field can be different because the tip−sample interaction affects the light coupling. For that, a Si photodetector precalibrated for the different wavelengths was placed in the location of the sample, and the probe was approached to mimic the conditions of the SCPM measurements. The power quoted in all captions refers to the power of the laser incident into the sample.

Conflict of Interest: The authors declare no competing financial interest.

Acknowledgment. The authors thank A. Band, M. Davanco, T. Landin, A. Myers, B. Nikoobakht, K. Srinivasan, J. Schumacher, K. Siebein, and all the CNST NanoFab staff. This work was partially supported by the Cooperative Research Agreement between the University of Maryland and the National Institute of Standards and Technology Center for Nanoscale Science and Technology, Award 70NANB10H193, through the University of Maryland. Sandia is a multiprogram laboratory operated by Sandia Corporation, a Lockheed Martin Company, for the U.S. DOE National Nuclear Security Administration under Contract DE-AC04-94AL85000.

Supporting Information Available: Structural characterization of the sculpted wedge, schematic of the experimental setup, and additional scanning photocurrent maps. This material is available free of charge *via* the Internet at http://pubs.acs.org.

REFERENCES AND NOTES

1. http://www.firstsolar.com/.
2. Green, M. A.; Emery, K.; Hishikawa, Y.; Warta, W.; Dunlop, E. D. Solar Cell Efficiency Tables (version 43). *Prog. Photovoltaics* **2014**, *22*, 1–9.
3. Shockley, W.; Queisser, H. J. Detailed Balance Limit of p-n Junction Solar Cells. *J. Appl. Phys.* **1961**, *32*, 510.
4. Nayak, P. K.; Bisquert, J.; Cahen, D. Assessing Possibilities and Limits for Solar Cells. *Adv. Mater.* **2011**, *23*, 2870–2876.
5. http://www.pv-tech.org.
6. Li, C.; Wu, Y.; Poplawsky, J.; Pennycook, T. J.; Paudel, N.; Yin, W.; Haigh, S. J.; Oxley, M. P.; Lupini, A. R.; Al-Jassim, M.; *et al.* Grain-Boundary-Enhanced Carrier Collection in CdTe Solar Cells. *Phys. Rev. Lett.* **2014**, *112*, 156103.
7. Galloway, S. A.; Brinkman, A. W.; Durose, K.; Wilshaw, P. R.; Holland, A. J. A Study of the Effects of Post-deposition Treatments on CdS/CdTe Thin Film Solar Cells Using High Resolution Optical Beam Induced Current. *Appl. Phys. Lett.* **1996**, *68*, 3725–3727.
8. Ringel, S. A.; Smith, A. W.; MacDougal, M. H.; Rohatgi, A. The Effects of $CdCl_2$ on the Electronic Properties of Molecular-Beam Epitaxially Grown CdTe/CdS Heterojunction Solar Cells. *J. Appl. Phys.* **1991**, *70*, 881–889.
9. Nakazawa, T.; Takamizawa, K.; Ito, K. High-Efficiency Indium Oxide Cadmium Telluride Solar-Cells. *Appl. Phys. Lett.* **1987**, *50*, 279–280.
10. Rose, D. H.; Hasoon, F. S.; Dhere, R. G.; Albin, D. S.; Ribelin, R. M.; Li, X. S.; Mahathongdy, Y.; Gessert, T. A.; Sheldon, P. Fabrication Procedures and Process Sensitivities for CdS/CdTe Solar Cells. *Prog. Photovoltaics* **1999**, *7*, 331–340.
11. Dobson, K. D.; Visoly-Fisher, I.; Hodes, G.; Cahen, D. Stability of CdTe/CdS Thin-Film Solar Cells. *Sol. Energy Mater. Sol. Cells* **2000**, *62*, 295–325.
12. Moutinho, H. R.; Dhere, R. G.; Jiang, C. S.; Al-Jassim, M. M.; Kazmerski, L. L. Electrical Properties of CdTe/CdS Solar Cells Investigated with Conductive Atomic Force Microscopy. *Thin Solid Films* **2006**, *514*, 150–155.
13. Moutinho, H. R.; Dhere, R. G.; Jiang, C. S.; Gessert, T.; Duda, A.; Young, M.; Metzger, W. K.; Al-Jassim, M. M. Role of Cu on the Electrical Properties of CdTe/CdS Solar Cells: A Cross-Sectional Conductive Atomic Force Microscopy Study. *J. Vac. Sci. Technol.* **2007**, *25*, 361–367.
14. Kumar, S. G.; Rao, K. S. R. K. Physics and Chemistry of CdTe/CdS Thin Film Heterojunction Photovoltaic Devices: Fundamental and Critical Aspects. *Energy Environ. Sci.* **2014**, *7*, 45–102.
15. McCandless, B. E.; Dobson, K. D. Processing Pptions for CdTe Thin Film Solar Cells. *Sol. Energy* **2004**, *77*, 839–856.
16. McCandless, B. E.; Birkmire, R. W. Analysis of Post Deposition Processing for CdTe/CdS Thin Film Solar Cells. *Sol. Cells* **1991**, *31*, 527–535.
17. Durose, K.; Asher, S. E.; Jaegermann, W.; Levi, D.; McCandless, B. E.; Metzger, W.; Moutinho, H.; Paulson, P. D.; Perkins, C. L.; Sites, J. R.; *et al.* Physical Characterization of Thin-Film Solar Cells. *Prog. Photovoltaics* **2004**, *12*, 177–217.
18. Ballif, C.; Moutinho, H. R.; Al-Jassim, M. M. Cross-Sectional Electrostatic Force Microscopy of Thin-Film Solar Cells. *J. Appl. Phys.* **2001**, *89*, 1418–1424.

19. Visoly-Fisher, I.; Cohen, S. R.; Cahen, D. Direct Evidence for Grain-Boundary Depletion in Polycrystalline CdTe from Nanoscale-Resolved Measurements. *Appl. Phys. Lett.* **2003**, *82*, 556–558.
20. Jaegermann, W.; Klein, A.; Mayer, T. Interface Engineering of Inorganic Thin-Film Solar Cells: Materials-Science Challenges for Advanced Physical Concepts. *Adv. Mater.* **2009**, *21*, 4196–4206.
21. Li, W.; Cohen, S. R.; Cahen, D. Effect of Chemical Treatments on nm-Scale Electrical Characteristics of Polycrystalline Thin Film Cu(In,Ga)Se_2 Surfaces. *Sol. Energy Mater. Sol. Cells* **2014**, *120*, 500–505.
22. Moutinho, H. R.; Dhere, R. G.; Jiang, C. S.; Yan, Y. F.; Albin, D. S.; Al-Jassim, M. M. Investigation of Potential and Electric Field Profiles in Cross Sections of CdTe/CdS Solar Cells Using Scanning Kelvin Probe Microscopy. *J. Appl. Phys.* **2010**, *108*, 074503.
23. Chopra, K. L.; Paulson, P. D.; Dutta, V. Thin-Film Solar Cells: An Overview. *Prog. Photovoltaics* **2004**, *12*, 69–92.
24. Hafemeister, M.; Siebentritt, S.; Albert, J.; Lux-Steiner, M. C.; Sadewasser, S. Large Neutral Barrier at Grain Boundaries in Chalcopyrite Thin Films. *Phys. Rev. Lett.* **2010**, *104*, 196602.
25. Galloway, S. A.; Edwards, P. R.; Durose, K. Characterisation of Thin Film CdS/CdTe Solar Cells Using Electron and Optical Beam Induced Current. *Sol. Energy Mater. Sol. Cells* **1999**, *57*, 61–74.
26. Takihara, M.; Minemoto, T.; Wakisaka, Y.; Takahashi, T. An Investigation of Band Profile Around the Grain Boundary of Cu(InGa)Se_2 Solar Cell Material by Scanning Probe Microscopy. *Prog. Photovoltaics* **2013**, *21*, 595–599.
27. Visoly-Fisher, I.; Cohen, S. R.; Gartsman, K.; Ruzin, A.; Cahen, D. Understanding the Beneficial Role of Grain Boundaries in Polycrystalline Solar Cells from Single-Grain-Boundary Scanning Probe Microscopy. *Adv. Funct. Mater.* **2006**, *16*, 649–660.
28. Visoly-Fisher, I.; Cohen, S. R.; Ruzin, A.; Cahen, D. How Polycrystalline Devices Can Outperform Single-Crystal Ones: Thin Film CdTe/CdS Solar Cells. *Adv. Mater.* **2004**, *16*, 879–883.
29. Herndon, M. K.; Gupta, A.; Kaydanov, V.; Collins, R. T. Evidence for Grain-Boundary-Assisted Diffusion of Sulfur in Polycrystalline CdS/CdTe Heterojunctions. *Appl. Phys. Lett.* **1999**, *75*, 3503–3505.
30. McDaniel, A. A.; Hsu, J. W. P.; Gabor, A. M. Near-Field Scanning Optical Microscopy Studies of Cu(In,Ga)Se_2 Solar Cells. *Appl. Phys. Lett.* **1997**, *70*, 3555–3557.
31. van Dyk, E. E.; Karoui, A.; La Rosa, A. H.; Rozgonyi, G. Near-Field Scanning Optical Microscopy for Characterisation of Photovoltaic Materials. *Phys. Status Solidi C* **2004**, *1*, 2292–2297.
32. McNeill, C. R.; Frohne, H.; Holdsworth, J. L.; Furst, J. E.; King, B. V.; Dastoor, P. C. Direct Photocurrent Mapping of Organic Solar Cells Using a Near-Field Scanning Optical Microscope. *Nano Lett.* **2004**, *4*, 219–223.
33. Mukhopadhyay, S.; Voggu, R.; Rao, C. N. R.; Vidhyadhiraja, N. S.; Narayan, K. S. Lateral Photocurrent Scanning of Donor and Acceptor Polymers on Graphene Coated Substrates. *Jpn. J. Appl. Phys.* **2011**, *50*, 061602.
34. Cojocaru-Miredin, O.; Choi, P.; Wuerz, R.; Raabe, D. Exploring the p-n Junction Region in Cu(In,Ga)Se_2 Thin-Film Solar Cells at the Nanometer-Scale. *Appl. Phys. Lett.* **2012**, *101*, 181603.
35. Yoon, H. P.; Haney, P. M.; Ruzmetov, D.; Xu, H.; Leite, M. S.; Hamadani, B. H.; Talin, A. A.; Zhitenev, N. B. Local Electrical Characterization of Cadmium Telluride Solar Cells Using Low-Energy Electron Beam. *Sol. Energy Mater. Sol. Cells* **2013**, *117*, 499–504.
36. Leite, M. S.; Abashin, M.; Lezec, H. J.; Gianfrancesco, A. G.; Talin, A. A.; Zhitenev, N. B. Mapping the Local Photoelectronic Properties of Polycrystalline Solar Cells through High Resolution Laser-Beam-Induced Current Microscopy. *IEEE J. Photovoltaics* **2014**, *4*, 311–316.
37. Smith, S.; Zhang, P.; Gessert, T.; Mascarenhas, A. Near-Field Optical Beam-Induced Currents in CdTe/CdS Solar Cells: Direct Measurement of Enhanced Photoresponse at Grain Boundaries. *Appl. Phys. Lett.* **2004**, *85*, 3854–3856.